RSC Advances




ROYAL SOCIETY OF CHEMISTRY

www.rsc.org/advances

RSC Advances

RSCPublishing

ARTICLE

# Scalable Synthesis of Two-dimensional Antimony Telluride Nanoplates Down to Single Quintuple Layer

Cite this: DOI: 10.1039/x0xx00000x

Fan Yang,[a] Robin B. Jacobs-Gedrim,[a] Mariyappan Shanmugam,[a] Nikhil Jain,[a] Michael T. Murphy,[a] Eui Sang Song,[a] David Frey,[b] and Bin Yu*,[a]

Received 00th January 2012,
Accepted 00th January 2012

DOI: 10.1039/x0xx00000x

www.rsc.org/

Scalable synthesis of two-dimensional topological insulators is critical to material exploration. We demonstrate controlled assembly of two-dimensional V-VI group compound $Sb_2Te_3$ nanoplates (NPs) through a vapor-solid growth process. The physical thickness of $Sb_2Te_3$ NPs can be rationally controlled in a wide range, from hundreds of nm down to sub-10 nm. Single-quintuple-layer $Sb_2Te_3$ NPs were obtained, with high domain density of ~$2.465 \times 10^8$ $cm^{-2}$ over a large surface area (1 cm × 1 cm) of $SiO_2$/Si substrate, verifying a scalable synthesis method. Extensive material analysis were conducted to explore the basic properties of $Sb_2Te_3$ NPs using SEM and AFM, etc. HRTEM confirms the NP samples exhibit a highly crystalline structure and XPS confirms the chemical composition and material stoichiometry. The growth of 2D topological insulator nanostructures may open up new opportunities in surface-state study and potential applications in low-dissipative electronic systems.

## Introduction

As the dimensions of traditional bulk materials decrease, basic physical properties varies due to quantum confinement and surface effects.[1] Two-dimensional (2D) atomic crystals are basic plane structure of bulk layered materials and have attracted significant attentions after graphene discovery.[2-4] A number of 2D nanostructures have been produced, including transitional metal dichalcogendes (TMDCs) (e.g., $MoS_2$)[5] and hexagonal boron nitride (h-BN).[6,7] Intriguing size-effect dependent properties have been reported in these materials, including non-conventional dielectric behavior[6,7], and tunable energy band-gaps[8]. We previously demonstrated extraordinary photoconductive behavior in 2D nanosheets.[9] The unique physical and chemical properties may lead to applications in electronics, photonics, catalytic chemistry, and energy harvesting.[10] $In_2Se_3$ nanosheets have an extremely high response to visible light, exhibiting a photoresponsivity of $3.95 \times 10^2$ $A \cdot W^{-1}$ at 300 nm with an external quantum efficiency greater than $1.63 \times 10^5$ % at 5 V bias.

Recently, a new family of layer-structured V-VI group compounds has been studied.[11,12] Topological insulators (TI) are a new class of materials in which the surface contains conducting states that behave drastically different from that of the insulating bulk.[13-15] While carrier conduction along the surface states are spin-polarized and protected by time-reversal symmetry, TIs potentially enable low-dissipative spintronics and quantum computing.[16] Unique phenomena such as ambipolar field effect, the Aharono-Bohm effect, and the Shubnikov-de Haas oscillation have been observed in ultrathin topological TIs.[17-19] Motivated by the potential advantages, we reported synthesis and electrical characteristics of $Bi_2Se_3$ nanoplates (NPs) and nanoribbons.[20] As compared with bulk topological insulator materials, ultrathin NPs especially single quintuple layer (QL), are highly preferable for studying conduction dominated by surface states due to the very large surface-to-volume ratio.[21,22] Controllable synthesis is an essential step toward exploitation and potential applications of 2D TI nanostructures.

Other than micromechanical exfoliation[15], multiple methods for the bottom-up assembly of ultra-thin NPs, including solvo-thermal synthesis[23], chemical vapor deposition[24], atomic layer deposition (ALD)[25] and molecular beam epitaxy (MBE)[21,26]. However, it is difficult for most of these synthesis processes to grow 10 or less QLs of TI materials directly on insulating substrate (e.g., $SiO_2$) which is desirable for TI property study and device implementation. Great challenges still exist in preparing scalable 2D structures in a controllable manner. To-date MBE process remains as the most effective method to achieve precise layer control.[29] Nevertheless, the technique is difficult and expensive. Developing a low-cost process to assemble ultrathin 2D NPs down to a-few-to-single QLs is highly desirable. In this work, we demonstrate a vapor-solid (VS) based method to synthesize 2D antimony telluride ($Sb_2Te_3$) NPs directly on $SiO_2$ surface with controlled thickness. For the first time, the growth of high-density single-QL $Sb_2Te_3$ NPs was made possible via the VS process. Moreover, the demonstrated synthesis method could be

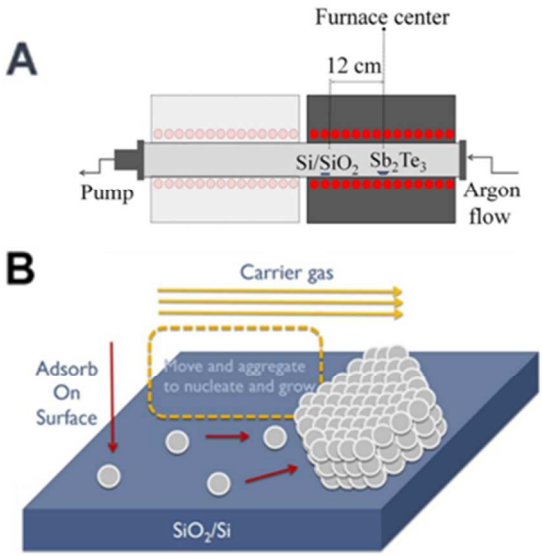


**Figure 1.** (A) Schematic diagram of the furnace used for the vapor-solid synthesis of $Sb_2Te_3$ NPs. (B) Growth mechanism of the major process sequence for the growth of $Sb_2Te_3$ NPs, including source flow and growth region thermal budget.

potentially extended to other 2D TI nanostructures in the binary sesquichalcogenide family.

## Experiments

### (A) Growth of $Sb_2Te_3$ Nanoplates

Figures 1A & 1B show the schematic of growth furnace and the thermal processing conditions during different phases of process, respectively. Bulk $Sb_2Te_3$ pieces (99.999% Alfa Aesar, 36282) were ground into powder and put into a quartz boat located in the center of furnace (Lindberg Blue M). The 1 × 1 $cm^2$ $SiO_2$/Si substrate was placed ~12 cm downstream from the furnace center. The furnace tube was sealed and pumped down to ~15 mTorr and subsequently flushed with ultra-pure argon several times prior to growth to remove environmental oxygen. We designed a quick ramping up and cooling down growth process to enable a rapidly increasing and decreasing temperature profile. The furnace was moved to the left and heated to over 500°C in 10 minutes and held at temperature for another 10 minutes, as shown in Figure 1A. In the meantime, 50 sccm to 100 sccm argon gas was introduced in the tube. Subsequently, during the growth step the furnace was moved to the right to position the source quartz boat in the furnace center, and evaporation and growth was initiated. The growth time was controlled to within 5 minutes due to relative fast deposition of $Sb_2Te_3$ on substrate. After the growth step, the furnace was moved away from source quartz boat and the $SiO_2$/Si substrate to initiate a quick cool down to room temperature in 30 minutes.

### (B) Material Characterization

The morphology was characterized by Scanning Electron Microscope (SEM, Hitachi S-4800) and Atomic Force Microscope (AFM, Veeco Dimension 3100 SPM) at tapping mode. Transmission Electron Microscope (TEM, JEOL 2010 Lab6 STEM) and X-ray Photoemission Spectroscopy (Thermo Scientific Theta Probe Angle-Resolved X-ray Photoelectron Spectrometer System) characterization were used to demonstrate crystal structure and chemical compositions of the as-synthesized NPs. Electronic measurement of ultrathin NPs was taken by Zyvex FIB/SEM sProber.

## Results and Discussion

Previous effort on synthesizing $Sb_2Te_3$ nanostructures using vapor-solid process has demonstrated hexagonal microplates and NPs with thicknesses of tens of nanometers.[28] The size and thickness of as-grown $Sb_2Te_3$ domains are mainly controlled by three important parameters: furnace temperature (T), argon flow rate ($J_{Ar}$), and growth time ($t$). In order to control the thickness of $Sb_2Te_3$ domains, we conducted experiments by using precursor flux and temperature to change the degree of supersaturation of antimony and telluride atoms on the surface of $SiO_2$/Si to yield ultra-thin NPs. After trying several recipes, we obtained isolated NPs rather than whole film at 550°C with 100 sccm of argon for 5 minutes growth time. The synthesized NPs were characterized by SEM and AFM. The SEM image of Figure 2A shows high density of as-grown hexagonal $Sb_2Te_3$ NPs. The average nanoplate size is ~4 μm with thickness all over 100 nm. The AFM image in the inset shows the height of ~287 nm. From the AFM data, we see that the surface of NP is atomically flat, indicating a supersaturating growth process.

To reduce the formation of adlayers, the flow rate was adjusted from 100 sccm to 50 sccm while keeping other parameters the same, as shown in Figure 2B. The as-grown NPs show an average size of ~8 μm, larger than during the growth with decreased flow rate. The AFM measurement confirms that the NP thickness mainly varies from 10 to 40 nm (10 nm thickness NP shown in Figure 2B inset). The hexagonal morphology indicates a highly crystalline structure which would be suitable for topological insulator surface study.[29] In addition, the hexagonal shape with flat surface suggest the growth of single crystalline $Sb_2Te_3$ NP (Figure 2B inset). Under this circumstance, surface-reaction-limited process is likely to dominate under lower pressure condition. Besides, higher gas velocity induces faster atomic migration on $SiO_2$/Si, resulting in less nucleation sites and more conformal deposition. Therefore, relatively larger size domains with less thickness were obtained.

From growth results discussed above, the VS growth of $Sb_2Te_3$ followed the Volmer-Weber island growth mode. Due to van der Waals bonding between neighboring quintuple layers, formation energy of adlayer $Sb_2Te_3$ is lower on as-grown NPs than on amorphous $SiO_2$ surface[30]. We choose $SiO_2$/Si substrate in this study. Note that quantity of vapor source during VS growth determines the NPs thickness. To reduce source supply, the growth duration was reduced to 4 minutes. The SEM image of the synthesized sample is shown in Figure 2C. Most of the NPs keep the same 120° edge angle with plate size ranging from to 500 nm ~ 3 μm. We noticed that with the reduction in time, an interesting effect occurs. From the AFM line-scan, a ~5 nm height is detected on NP edge with ~10 nm height in the center region. Other than thickness, it appears that these NPs have wrinkled edges. Unlike step-by-step adlayer growth[31], the AFM line-scan data shows smooth elevation from edge to center. We assume the existence of a smaller thin plate underneath the large triangle-shaped 5 nm thick NPs. Ripples and wrinkled edges indicate that a smaller domain nucleated and growth, while the top layers were able to be formed before the growth of bottom layer is completed.

RSC Advances

RSCPublishing

ARTICLE

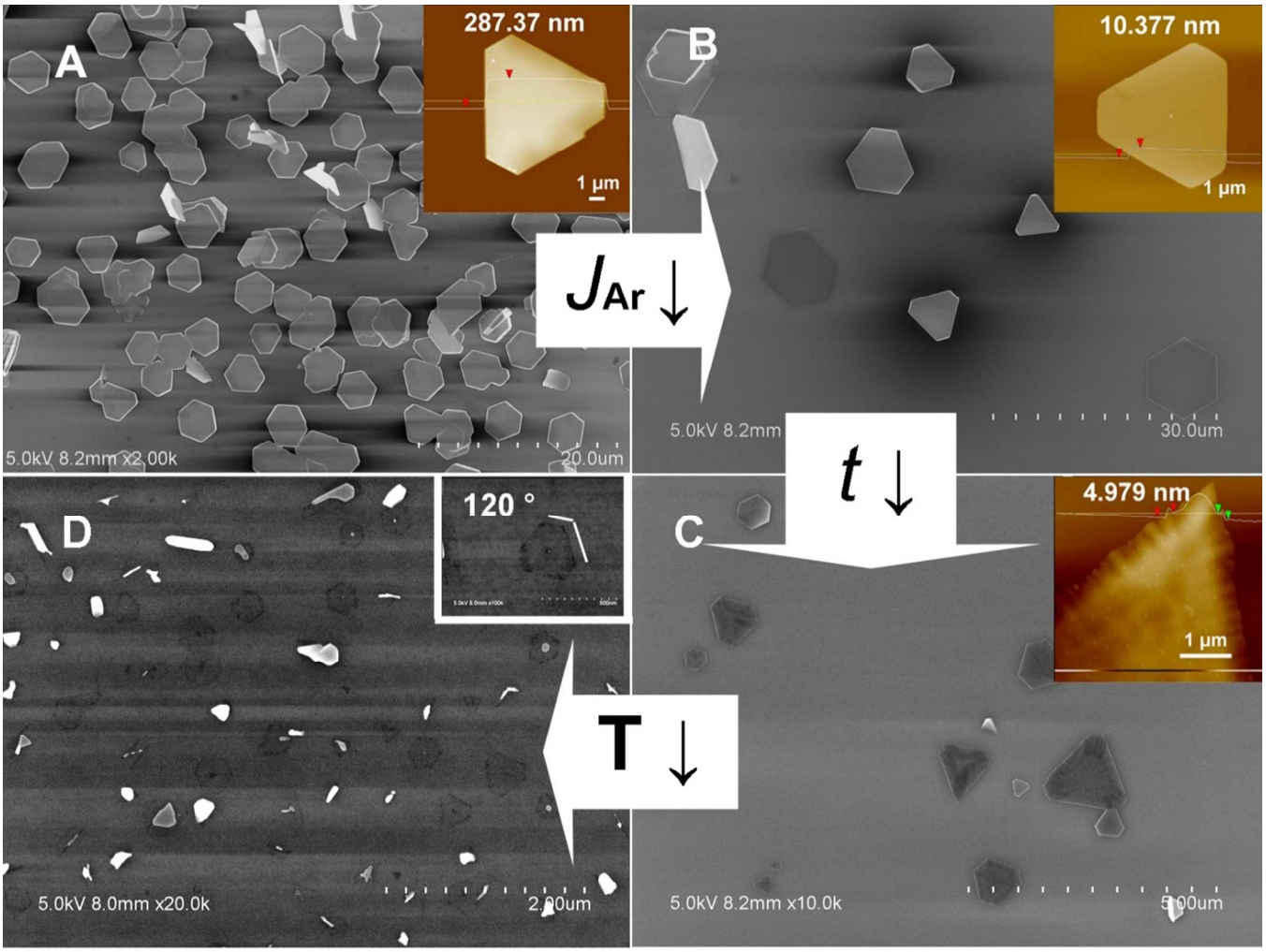


**Figure 2.** SEM images (with inset showing AFM images) of $Sb_2Te_3$ NPs assembled under different conditions: Temperature (°C)/ flow rate (sccm)/ reaction time (minute): (A) 550/100/5, (B) 550/50/5, (C) 550/50/4, and (D) 510/50/4.

According to the mechanism of chemical vapor deposition, deposition rate is inversely proportional to temperature. To further optimize the growth process, we reduced the furnace temperature to 510°C as shown in Figure 2D, while keeping the other conditions the same, as shown in Figure 2C. Thicker plates with lighter contrast were clearly seen with varying surface morphology. Besides, when higher magnitude of SEM (×20.0K or more) were conducted, a large amount of uniformly distributed NPs with dimensions of several hundred nanometers were found. We noticed that these plates were largely in hexagonal or triangular shape, while the micrographic contrast is only a bit darker than that from the substrate. These ultrathin NPs show an opposite contrast in SE2 imaging than thicker NPs, with a lower secondary electron yield than the substrate background. This is due to the generation of all the secondary electrons being within the sample substrate, and the presence of ultra-thin layers absorbing secondary electrons, whereas in a thicker plate, the cross-section of the secondary yield lies within the plate itself.

More characterization efforts were made to prove the assumption. First, high-resolution SEM images were acquired, as shown in Figures 3A and 3B. From the SEM images, sharp edges and 120° facets were clearly seen, indicating layer-structured rhombohedral-lattice crystal of $Sb_2Te_3$ (space group $D_{53d}$, R3m).[32,33] To verify the thickness of these ultrathin structures, AFM was employed to demonstrate the monolayer thickness of the nanoplates as shown in Figures 3C and 3D. From the line profiling results, a step height of 0.921 nm and 1.063 nm is observed, although large surface roughness is seen on the $SiO_2$/Si substrate. Unlike mono-layer graphene which

RSC Advances RSCPublishing

ARTICLE

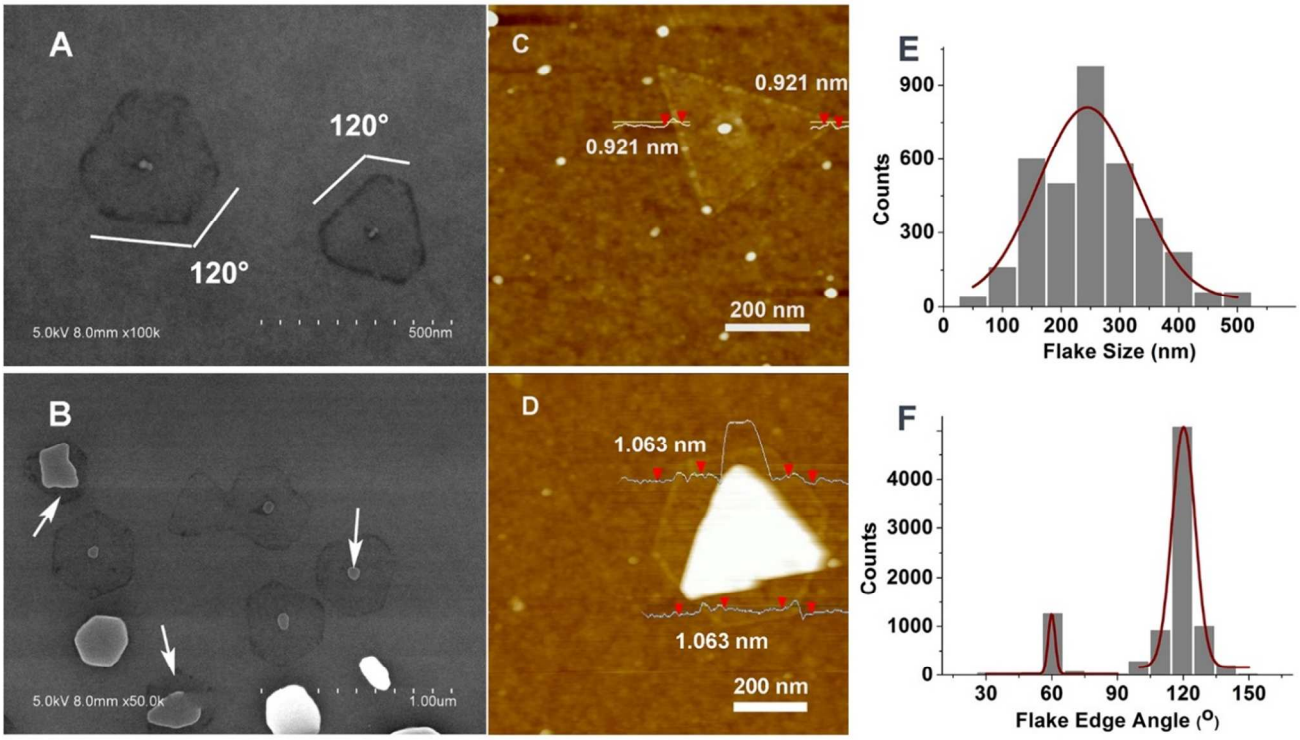


**Figure 3.** (A) & (B) SEM image of $Sb_2Te_3$ NPs. AFM image of (C) single-QL $Sb_2Te_3$ NP and (D) $Sb_2Te_3$ NP with underneath the single-QL region. (E) & (F) show the statistics of domain size and edge angle of the single-QL $Sb_2Te_3$ NPs, respectively.

consist only one atom thickness, a single five atom thick quintuple layer of $Sb_2Te_3$ is ~ 1 nm in Z thickness. Therefore, the ultrathin $Sb_2Te_3$ NPs is verified to be a single QL. This further demonstrating the preferential epitaxy process for $Sb_2Te_3$, as discussed above. A statistical study of the edge morphology of the single QL NPs was performed by selecting a 50 μm × 50 μm square area. Figure 3E and 3F show the histograms of the NP size and edge angle, which help to confirm the crystal structure. The domain size varies in the range of 100 nm to 400 nm. With fitting curve on the statistical data, the average domain size is ~250 nm. To calculate the single-QL domain coverage, we took total 49 SEM images across the 1 $cm^2$ $SiO_2$/Si substrate, using an array of 7 x 7 square dots with the distance between neighboring dots about 1.35 mm. We then calculated the NP yield based on the SEM images (with 20,000X magnitude). The average domain count is ~44.364 per image (area: 5 μm × 3.6 μm). The density is thus 2.465 x $10^8$ $cm^{-2}$. Note this does not include larger blobs as shown in Figure 3D. Although domain density is high, the coverage of the single-QL domains is only 13.3%.We attributed it to small average domain size. Since the growth substrate is $SiO_2$/Si possessing amorphous surface, it is expected to form $Sb_2Te_3$ with several times larger size on a layered mica substrate through van der Waals epitaxy process.[33] We'll explore other possible ways to obtain larger single-QL domains in the next phase of research. Figure 3F illustrates the facets angle of single-QL NPs. From the statistic results and fitting curves, 60° or 120° facets were seen at most of domain edges, as expected from the crystal structure.[34]

Besides analysing domain morphology, it is noted that the small dots located at the center of the single-QL $Sb_2Te_3$ NPs could serve as the nucleation site during the growth process. With excessive source atoms deposited onto the nucleation site to form $Sb_2Te_3$ NPs, thicker layers were formed on top of the ultrathin plates, as shown in Figure 3B. It is worth noting that the adlayer region never exceeds the single-QL region. And no matter what recipe we changed during our growth process, the size of these single QL NPs will never increase in size but only in thickness. It seems that the role of these $Sb_2Te_3$ NPs were the basic structure for upper layer growth due to lower energy for forming $Sb_2Te_3$ layers on top of ultrathin NPs. Epitaxial process dominate growth of $Sb_2Te_3$ NPs after forming of these ultrathin layers. What's more, by comparing with previous samples Figure 2B and 2C, a different mechanism of ultrathin $Sb_2Te_3$ growth is proposed: first of all, single QL $Sb_2Te_3$ NPs were formed through atoms deposition and migration on top of $SiO_2$/Si surface. However, due to lattice mismatch between $SiO_2$/Si and $Sb_2Te_3$, the size of NPs was limited to hundreds of nanometers. After first layer forming, adlayer will preferably grow on top of single QL NPs layer by layer. Sequent in

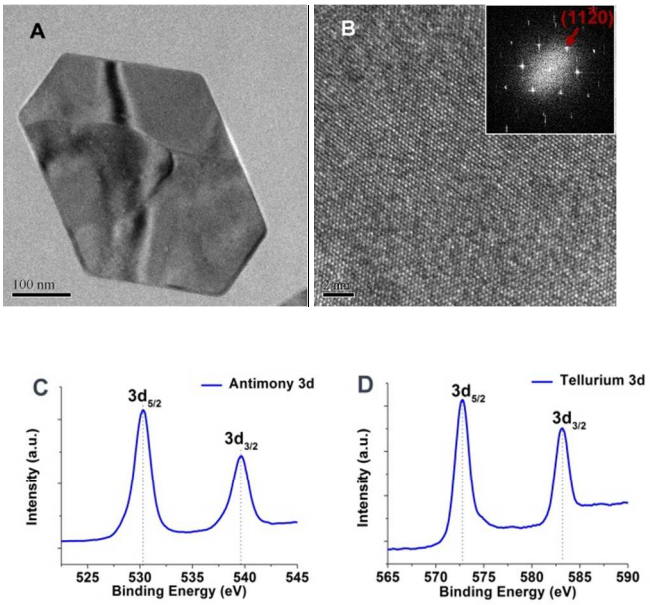


**Figure 4.** (A) Low-magnification TEM image of single $Sb_2Te_3$ NP on $Si_3N_4$ grid substrate. (B) HRTEM of $Sb_2Te_3$ NP in (A). Upper inset is the corresponding indexed FFT pattern; XPS results for (C) antimony 3d curve and (D) telluride 3d curve measured from the $Sb_2Te_3$ NPs on $SiO_2$/Si substrate.

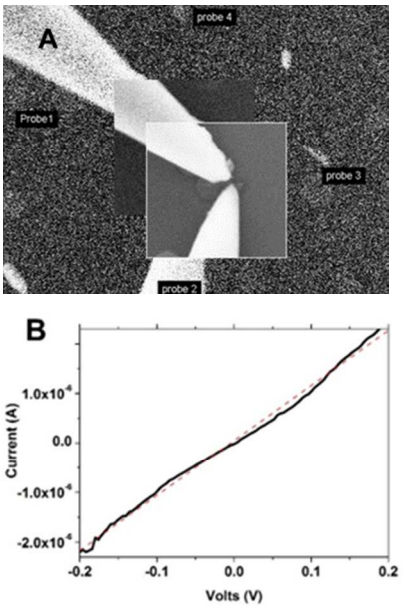


**Figure 5.** (A) Low-magnification TEM image showing the contact probes down to the single-QL $Sb_2Te_3$ NP in the electrical testing. (B) Measured current-voltage characteristics of the single-QL $Sb_2Te_3$ NP.

specific layer thickness, the epitaxial upper layer grow larger and start exceeding the size to microns (Figure 2C). Then, lower layers will grow larger, reversely epitaxial from upper layer NPs. Therefore, the homogeneous thickness of $Sb_2Te_3$ NPs were grown on top of $SiO_2$/Si substrate. So far, we are not able to prove our assumption on the growth mechanism. Further study will require *in-situ* growth observation tools such as low-energy electron microscope (LEEM).

In addition to morphology analysis, TEM and XPS were performed to measure the crystal structure and chemical composition of the as-synthesized NPs. Since the small plate size makes it difficult to be transferred onto the traditional holey grid, we used silicon nitride ($Si_3N_4$) TEM grid as the substrate for $Sb_2Te_3$ growth, along with $SiO_2$/Si substrate. Figure 4A shows the low-magnification TEM image of a single $Sb_2Te_3$ NP directly grown on $Si_3N_4$ grid substrate such that the NP could be imaged without a transfer process. Similar to SEM results, the plate exhibit hexagonal shape with all 120° facet at the edges. In order to study the detailed crystalline feature of the $Sb_2Te_3$ domains, we conducted high resolution transmission electron microscope (HRTEM) and the corresponding Fast Fourier Transform (FFT) image, as shown in Figure 4B. A well-defined hexagonal lattice fringes can be clearly seen without apparent defects. It is worth noting that, since the synthesized NPs were very thin, the amorphous $Si_3N_4$ substrate will influence the imaging results.[22,35] The single-spot diffraction in the FFT pattern indicates the formation of single crystalline NP. The atomic spacing (0.213 nm) is consistent with the lattice characteristic of $Sb_2Te_3$ in [$1\bar{1}\bar{2}0$ ].[36]

We further conducted XPS elemental analysis. Figures 4C and 4D show the high-resolution XPS spectra of antimony 3d and telluride 3d region, respectively. From Figure 3C, two strong peaks at 530.3 eV and 539.0 eV are assigned to Sb ($3d_{5/2}$) and Sb ($3d_{3/2}$), respectively. The peaks at 572.7 eV and 583 eV are associated with Te ($3d_{5/2}$) and Te ($3d_{3/2}$), respectively, as illustrated in Figure 3D.[37] These observed peaks demonstrate crystal structure of the synthesized NPs and agree well with the previously reported results. Additionally, we calculated the elemental ratio through XPS data after subtracting silicon oxide substrate. The result of elemental antimony and tellurium ratio is 2:2.95, fitting the stoichiometric of $Sb_2Te_3$. It is worth noting that a small amount of oxygen (~6%) and carbon (~4%) is detected in our samples. We attributed it to surface contamination after the sample was taken out from CVD furnace and exposed to air. Additionally, the oxygen is not only from contamination due to ambient exposing. Negligible bumps at ~578.0 eV and ~587.0 eV were detected, as shown in Figure 4D, indicating the existence of very few oxygen-tellurium bonding.

The current-voltage (I-V) measurements were conducted to explore the basic electrical behavior of the synthesized samples. As the $Sb_2Te_3$ NPs are small, we directly probed down onto the resistance of the obtained NPs by using Zyvex SEM tool. The I-V curve recorded from the sample (Figure 5B) shows a nearly linear relationship with an electrical resistance of ~90 K Ohms, indicating an Ohmic contact between the probe and the $Sb_2Te_3$ NP sample. The conductivity of as-grown NPs are not high as expected bulk topological insulator. We attributed it to high contact resistance. What's more, it is possible that with opening Dirac cone for ultrathin NPs, electrical conductivity will be influenced as well. Future works will be focused on larger domain growth and facile larger electronic devices fabrication. Thus, more electronic properties will be detected more accurately, while phenomenon of opening Dirac cone of surface state will be expected.

## Conclusions

In summary, we demonstrated the rational growth of high-density two-dimensional $Sb_2Te_3$ NPs with variable physical thickness through a vapor-solid process. The thickness control of the synthesized $Sb_2Te_3$ NPs down to a single-quintuple-layer has been proved to be possible. The $Sb_2Te_3$ NPs are in highly crystalline phase, covering the surface of $SiO_2$/Si substrate. The 2D TI nanostructures with ultra-large surface-to-volume ratio could serve as the ideal material platform for studying surface-state conducting behaviour and possible realization of ultra-low-dissipative electronics.

## Acknowledgements

The research work was partially supported by National Science Foundation (grants No. 1162312 and 1434689).

## References

1. E. Roduner, *Chemical Society reviews*, 2006, 35, 583-592.
2. K. Novoselov, A. K. Geim, S. Morozov, D. Jiang, M. K. I. Grigorieva, S. Dubonos and A. Firsov, *Nature*, 2005, 438, 197-200.
3. K. S. Novoselov, Z. Jiang, Y. Zhang, S. Morozov, H. Stormer, U. Zeitler, J. Maan, G. Boebinger, P. Kim and A. Geim, *Science*, 2007, 315, 1379-1379.
4. K. S. Novoselov, A. K. Geim, S. Morozov, D. Jiang, Y. Zhang, S. Dubonos, I. Grigorieva and A. Firsov, *Science*, 2004, 306, 666-669.
5. Y. H. Lee, X. Q. Zhang, W. Zhang, M. T. Chang, C. T. Lin, K. D. Chang, Y. C. Yu, J. T. W. Wang, C. S. Chang and L. J. Li, *Advanced materials*, 2012, 24, 2320-2325.
6. K. K. Kim, A. Hsu, X. Jia, S. M. Kim, Y. Shi, M. Dresselhaus, T. Palacios and J. Kong, *ACS nano*, 2012, 6, 8583-8590.
7. K. K. Kim, A. Hsu, X. Jia, S. M. Kim, Y. Shi, M. Hofmann, D. Nezich, J. F. Rodriguez-Nieva, M. Dresselhaus, T. Palacios and J. Kong, *Nano letters*, 2012, 12, 161-166.
8. B. Radisavljevic, A. Radenovic, J. Brivio, V. Giacometti and A. Kis, *Nature nanotechnology*, 2011, 6, 147-150.
9. R. B. Jacobs-Gedrim, M. Shanmugam, N. Jain, C. A. Durcan, M. T. Murphy, T. M. Murray, R. J. Matyi, R. L. Moore and B. Yu, *ACS nano*, 2013, 8, 514-521.
10. D. C. Elias, R. R. Nair, T. M. Mohiuddin, S. V. Morozov, P. Blake, M. P. Halsall, A. C. Ferrari, D. W. Boukhvalov, M. I. Katsnelson, A. K. Geim and K. S. Novoselov, *Science*, 2009, 323, 610-613.
11. D. Hsieh, D. Qian, L. Wray, Y. Xia, Y. S. Hor, R. Cava and M. Z. Hasan, *Nature*, 2008, 452, 970-974.
12. D. Hsieh, Y. Xia, L. Wray, D. Qian, A. Pal, J. Dil, J. Osterwalder, F. Meier, G. Bihlmayer and C. Kane, *Science*, 2009, 323, 919-922.
13. P. Hosseini, C. D. Wright and H. Bhaskaran, *Nature*, 2014, 511, 206-211.
14. M. Z. Hasan and C. L. Kane, *Reviews of Modern Physics*, 2010, 82, 3045.
15. J. Checkelsky, Y. Hor, R. Cava and N. Ong, *Physical review letters*, 2011, 106, 196801.
16. Q.-K. Xue, *Nature nanotechnology*, 2011, 6, 197-198.
17. H. Peng, K. Lai, D. Kong, S. Meister, Y. Chen, X.-L. Qi, S.-C. Zhang, Z.-X. Shen and Y. Cui, *Nature materials*, 2010, 9, 225-229.
18. T.-C. Chiang, *Surface Science Reports*, 2000, 39, 181-235.
19. H.-Z. Lu, W.-Y. Shan, W. Yao, Q. Niu and S.-Q. Shen, *Physical review B*, 2010, 81, 115407.
20. R. B. Jacobs-Gedrim, C. A. Durcan, N. Jain and B. Yu, *Applied Physics Letters*, 2012, 101, 143103.
21. G. Wang, X. Zhu, J. Wen, X. Chen, K. He, L. Wang, X. Ma, Y. Liu, X. Dai and Z. Fang, *Nano Research*, 2010, 3, 874-880.
22. D. Kong, W. Dang, J. J. Cha, H. Li, S. Meister, H. Peng, Z. Liu and Y. Cui, *Nano letters*, 2010, 10, 2245-2250.
23. Checkelsky, J.; Hor, Y.; Cava, R.; Ong, N. *Physical review letters* 2011, 106, 196801.
24. S. S. Garje, D. J. Eisler, J. S. Ritch, M. Afzaal, P. O'Brien and T. Chivers, *Journal of the American Chemical Society*, 2006, 128, 3120-3121.
25. G. Bendt, S. Zastrow, K. Nielsch, P. S. Mandal, J. Sánchez-Barriga, O. Rader and S. Schulz, *Journal of Materials Chemistry A*, 2014, 2, 8215-8222.
26. L. Zheng, X. Cheng, D. Cao, Q. Wang, Z. Wang, C. Xia, L. Shen, Y. Yu and D. Shen, *RSC Advances*, 2015.
27. Y. Zhang, K. He, C.-Z. Chang, C.-L. Song, L.-L. Wang, X. Chen, J.-F. Jia, Z. Fang, X. Dai and W.-Y. Shan, *Nature Physics*, 2010, 6, 584-588.
28. G. Hao, X. Qi, G. Wang, X. Peng, S. Chang, X. Wei and J. Zhong, *RSC Advances*, 2012, 2, 10694-10699.
29. H. Li, J. Cao, W. Zheng, Y. Chen, D. Wu, W. Dang, K. Wang, H. Peng and Z. Liu, *Journal of the American Chemical Society*, 2012, 134, 6132-6135.
30. Y. Y. Li, G. Wang, X. G. Zhu, M. H. Liu, C. Ye, X. Chen, Y. Y. Wang, K. He, L. L. Wang and X. C. Ma, *Advanced materials*, 2010, 22, 4002-4007.
31. Y. Yan, Z.-M. Liao, Y.-B. Zhou, H.-C. Wu, Y.-Q. Bie, J.-J. Chen, J. Meng, X.-S. Wu and D.-P. Yu, *Scientific reports*, 2013, 3.
32. M. Lin, D. Wu, Y. Zhou, W. Huang, W. Jiang, W. Zheng, S. Zhao, C. Jin, Y. Guo, H. Peng and Z. Liu, *Journal of the American Chemical Society*, 2013, 135, 13274-13277.
33. J. S. Lee, S. Brittman, D. Yu and H. Park, *Journal of the American Chemical Society*, 2008, 130, 6252-6258.
34. S. Souza, C. Poffo, D. Trichês, J. De Lima, T. Grandi, A. Polian and M. Gauthier, *Physica B: Condensed Matter*, 2012, 407, 3781-3789.
35. A. Vargas, S. Basak, F. Liu, B. Wang, E. Panaitescu, H. Lin, R. Markiewicz, A. Bansil and S. Kar, *ACS nano*, 2014, 8, 1222-1230.
36. W. Wang, W. Wang, B. Poudel, J. Yang, D. Wang and Z. Ren, *Journal of the American Chemical Society*, 2005, 127, 13792-13793.